RESEARCH ARTICLE

NEUROSCIENCE

Retrograde endocannabinoid signaling at inhibitory synapses in vivo

Barna Dudok[1,2]*†, Linlin Z. Fan[3]†, Jordan S. Farrell[2,4,5], Shreya Malhotra[2], Jesslyn Homidan[2], Doo Kyung Kim[3], Celestine Wenardy[3], Charu Ramakrishnan[6], Yulong Li[7], Karl Deisseroth[3,8,9], Ivan Soltesz[2]

Endocannabinoid (eCB)–mediated suppression of inhibitory synapses has been hypothesized, but this has not yet been demonstrated to occur in vivo because of the difficulty in tracking eCB dynamics and synaptic plasticity during behavior. In mice navigating a linear track, we observed location-specific eCB signaling in hippocampal CA1 place cells, and this was detected both in the postsynaptic membrane and the presynaptic inhibitory axons. All-optical in vivo investigation of synaptic responses revealed that postsynaptic depolarization was followed by a suppression of inhibitory synaptic potentials. Furthermore, interneuron-specific cannabinoid receptor deletion altered place cell tuning. Therefore, rapid, postsynaptic, activity-dependent eCB signaling modulates inhibitory synapses on a timescale of seconds during behavior.

Strong depolarization of neurons can induce a transient suppression of their inhibitory synaptic inputs in acute brain slices (*1*, *2*). Such retrograde, activity-dependent suppression of GABAergic synapses, referred to as depolarization-induced suppression of inhibition (DSI), is mediated by endocannabinoid (eCB) signaling (*3*–*5*). In vitro studies have shown that robust postsynaptic calcium (post-Ca) increase during DSI triggers eCB synthesis and the retrograde activation of cannabinoid type-1 receptors (CB_1s), which in turn suppresses GABA release. In the CA1 region of the hippocampus, the highest CB_1 expression is found on axons of perisomatically projecting GABAergic basket cells that also express cholecystokinin (CCKBCs) (*6*–*8*). Conversely, the other major basket cell type, parvalbumin-expressing basket cells (PVBCs), do not express CB_1s. Correspondingly, DSI is maximally potent at CCKBC inputs to pyramidal cells and is capable of completely muting these synapses (*9*, *10*).

DSI has been hypothesized to also occur in vivo, but the specific neuronal activity patterns that give rise to DSI remain unknown (*11*). When mammals navigate their environment, individual hippocampal pyramidal cells discharge at specific place fields (*11*, *12*), and several observations are consistent with the possibility that place cell firing in behaving animals may engage a DSI-like phenomenon. In vitro, externally imposed place cell–like activity can drive DSI (*13*), and disinhibition of the postsynaptic cells by DSI can facilitate excitatory synapse plasticity (*14*, *15*). In vivo, place cell formation is supported by reduced inhibition (*16*, *17*). A potential role of DSI in hippocampal place field properties has been proposed

[1]Departments of Neurology and Neuroscience, Baylor College of Medicine, Houston, TX 77030, USA. [2]Department of Neurosurgery, Stanford University, Stanford, CA 94305, USA. [3]Department of Bioengineering, Stanford University, Stanford, CA 94305, USA. [4]F.M. Kirby Neurobiology Center and Rosamund Stone Zander Translational Neuroscience Center, Boston Children's Hospital, Boston, MA 02115, USA. [5]Department of Neurology, Boston Children's Hospital, Harvard Medical School, Boston, MA 02115, USA. [6]Cracking the Neural Code (CNC) Program, Stanford University, Stanford, CA 94305, USA. [7]State Key Laboratory of Membrane Biology, School of Life Sciences, Peking University, Beijing 100871, China. [8]Department of Psychiatry and Behavioral Sciences, Stanford University, Stanford, CA 94305, USA. [9]Howard Hughes Medical Institute, Stanford, CA 94305, USA.
***Corresponding author. Email: barna.dudok@bcm.edu**
†These authors contributed equally to this work.

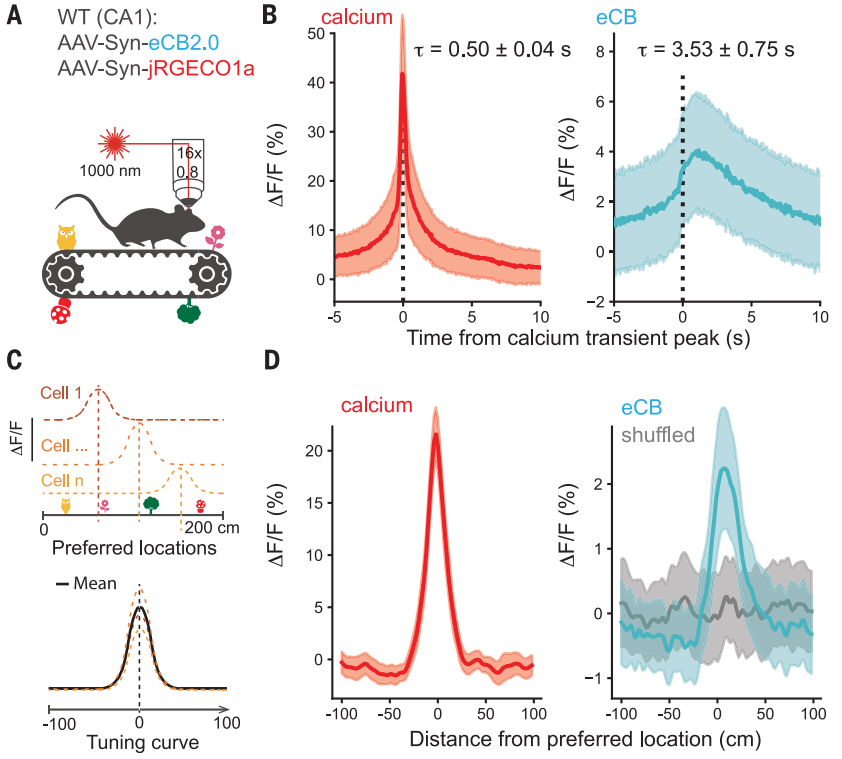

Fig. 1. Rapid eCB signaling in the hippocampus in vivo. (**A**) $GRAB_{eCB2.0}$ and jRGECO1a were expressed in CA1 neurons. Head-fixed mice ran on a linear treadmill during multiphoton imaging. (**B**) Event-aligned average single-cell calcium and eCB responses during calcium transients. Plot shows mean responses (line) ± SEM (shaded area) for n = 4 sessions from n = 4 vehicle-treated mice, 607 ± 241 ROIs per session, and 5.2 ± 1.1 peaks per ROI. Labels show decay time constants of exponential fits. (**C**) Analysis of place cells. Average tuning curves (solid black line) were calculated for each session by aligning location-averaged place cell traces on their preferred location. (**D**) Average spatial tuning curves (±SEM) are shown centered on the preferred location of place cells (red indicates calcium) together with the tuning curves of eCB signals from the same cells (blue) or after shuffling cells within sessions (gray). One-sided, one-sample t test with alternative hypothesis $\mu > 0$: $P = 5.67 \times 10^{-5}$, n = 4 male mice; shuffle: $P = 0.88$. Plots show average tuning curves (line) ± SEM (shaded area), n = 4 sessions from n = 4 drug-naïve mice and 161 ± 35 place cell ROIs per session.

(*18*); however, the steps that would underlie a retrograde, eCB-mediated, DSI-like plasticity in vivo have remained speculative, and the hypothesis that DSI contributes to place cell disinhibition has remained untested. Here, we used optical methods in mice navigating a linear track to test (i) whether place cell activity in behaving animals is sufficient to trigger eCB synthesis in the postsynaptic cell, (ii) whether eCB signals affect presynaptic CB_1s on GABAergic terminals in vivo, and (iii) whether DSI-like plasticity can modulate place cell activity patterns.

Location-specific eCB signaling by place cells

The genetically encoded G protein–coupled receptor activation based eCB reporter $GRAB_{eCB2.0}$ enables the recording of eCB dynamics with high spatial resolution in vivo (*19*, *20*). eCB mobilization during DSI depends on post-Ca influx (*21*). To characterize eCB signaling related to calcium transients, we expressed $GRAB_{eCB2.0}$ and the red-shifted calcium sensor jRGECO1a (*22*) in CA1 neurons. We performed two-photon dual calcium and eCB imaging in the pyramidal layer while mice ran several laps on a linear treadmill track with tactile cues (Fig. 1A) (*23*). We segmented regions of interest (ROIs) corresponding to neuronal somata (most of which in the pyramidal layer are expected to belong to pyramidal cells) (*24*) and measured calcium and eCB signals in the same ROIs. We analyzed calcium transients by finding peaks on traces of fluorescence change over baseline ($\Delta F/F$) (Fig. 1B). Transient eCB signals were detected concomitant with calcium peaks (Fig. 1B), with a peak delayed by 1.04 ± 0.16 s relative to calcium and an average decay time constant of 3.53 ± 0.75 s. To investigate which eCB ligand contributes to the transients, we performed the latter analysis on datasets that we previously recorded in the presence of ligand-specific inhibitors of eCB synthesis or metabolism (*20*). Calcium peak–coupled eCB transients were suppressed by inhibiting the synthesis of 2-arachidonoylglycerol (2-AG), the eCB species involved in CA1 DSI in vitro (*25*). Furthermore, eCB transient durations were extended after we treated mice with JZL 184 to inhibit monoacylglycerol lipase (MGL) and thus 2-AG degradation (*25*, *26*) (fig. S1, A to C). Conversely, manipulations altering the synthesis or degradation of the other major eCB species, anandamide (AEA), had no effect on the in vivo eCB transients (fig. S1, D to F).

Next, to investigate eCB dynamics specifically in place cells, we identified place cells by calculating location-specific average calcium signals (Fig. 1C). Average eCB signals were elevated around the same track locations where calcium was high in the same individual place cells (Fig. 1D). These results indicate that eCB mobilization in place cells during exploration is specific to the cell's preferred location. By contrast, non-place cells had lower calcium and accompanying eCB transient amplitudes compared with place cells in the same field of view (fig. S1G).

Although the molecular mechanisms of retrograde eCB transport are not precisely understood, there is general agreement that DSI requires the postsynaptically generated eCBs to engage presynaptic CB_1s on interneuronal terminals impinging on the activated neuron (*4*, *27*). Thus, we specifically allowed the expression of $GRAB_{eCB2.0}$ only in interneurons using Dlx5/6-Cre transgenic mice (*28*) to enable presynaptic eCB measurements (fig. S2A). The distribution of $GRAB_{eCB2.0}$, a chimera of CB_1 and a green fluorescent protein variant, resembled membrane-enriched CB_1 targeting (*29*) in interneuron axon terminals, with no detectable postsynaptic expression in principal cells and relatively low expression in interneuron somata (fig. S2, B to F).

For simultaneously imaging somatic calcium and axonal eCB transients, we combined interneuronal $GRAB_{eCB2.0}$ and pan-neuronal, red-shifted calcium sensor expression (Fig. 2A and fig. S2E). We generated somatic, putatively post-Ca ROI sets as above and measured nearby axonal, putatively presynaptic eCB (pre-eCB) signals after enlarging the somatic

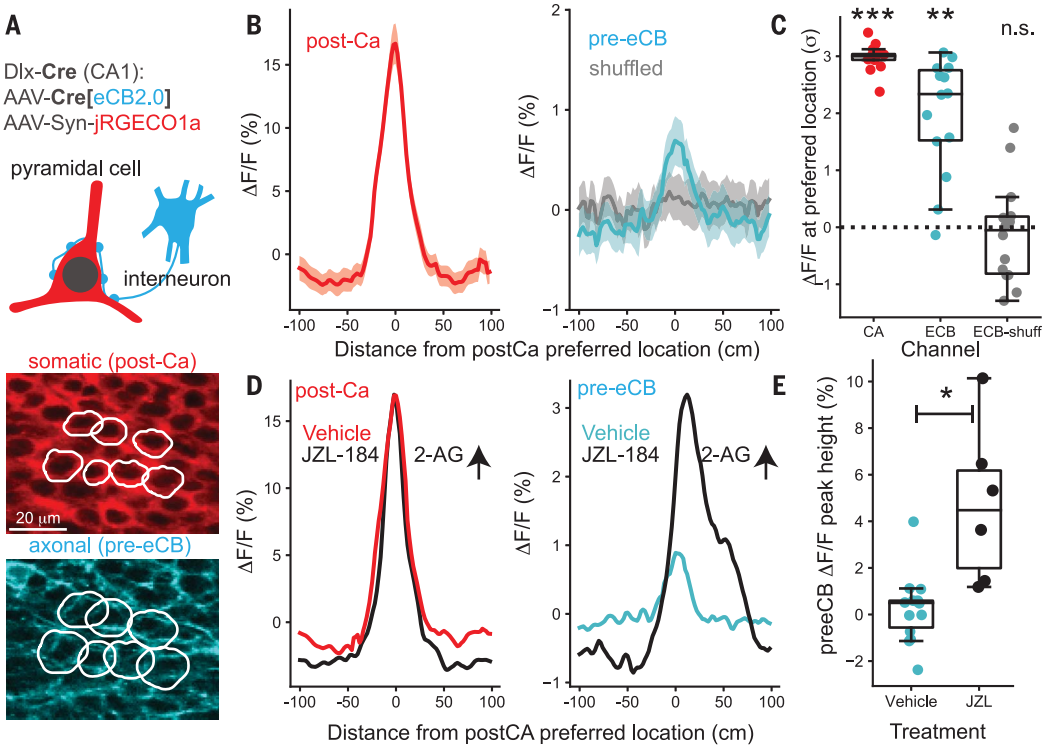

Fig. 2. Spatially tuned presynaptic eCB signals in the hippocampus in vivo. (**A**) Labeling strategy for in vivo imaging. Interneuronal $GRAB_{eCB2.0}$ and pan-neuronal jRGECO1a expression were combined. Bottom panels show the segmentation approach. Neuron cell bodies were segmented in the jRGECO1a channel (post-Ca). The ROIs were enlarged by binary dilation for measuring signals in the neighboring axons in the $GRAB_{eCB2.0}$ channel (pre-eCB). (**B**) Average spatial tuning curves (±SEM) are shown centered on the preferred location of place cells (red indicates calcium) together with the tuning curves of eCB signals from the corresponding pre-eCB ROIs (blue) or after shuffling ROIs within sessions (gray), n = 18 sessions from n = 5 mice and 193 ± 130 ROIs per session. (**C**) Quantification of signal intensity at the preferred location. Boxes indicate median ± interquartile range; whiskers: nonoutlier range; markers: recording sessions. pre-eCB: P = 0.002, n = 5 mice (n = 3 males and n = 2 females); shuffle: P = 0.69. (**D**) Spatial tuning curves are shown after injecting mice with JZL-184 to inhibit the enzymatic breakdown of the eCB 2-AG by MGL or after vehicle injection. (**E**) Quantification of location-specific pre-eCB signals, P = 0.0004, Mann-Whitney test, n = 14 vehicle sessions from n = 5 mice and n = 6 JZL sessions from n = 3 mice.

ROIs (Fig. 2A). Similar to eCB signals measured in place cell somata (Fig. 1D), pre-eCB signals in interneuronal axons surrounding place cells were elevated at the same track locations where post-Ca was high (Fig. 2, B and C). These results indicate that place cell activations during behavior are accompanied by eCB signaling at perisomatic inhibitory axons.

Similarly to DSI in vitro (*30*) and calcium transient–related post-eCB signals in vivo (fig. S1B), location-specific pre-eCB signals around place cells were magnified by pharmacological inhibition of 2-AG degradation (Fig. 2, D and E), consistent with a prominent role of 2-AG in inhibitory axon eCB signaling while not ruling out the partial involvement of other eCBs such as AEA.

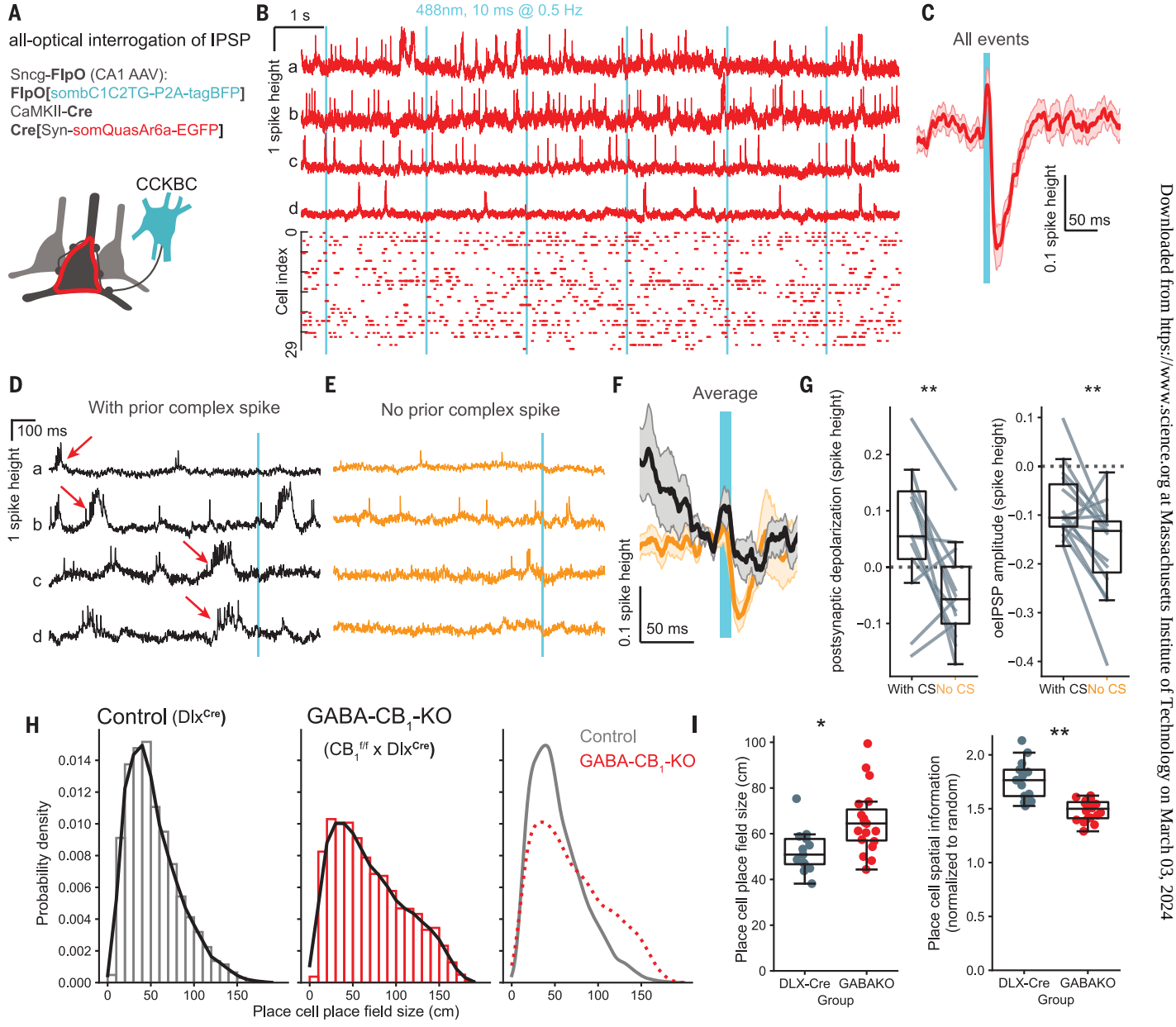

Fig. 3. Inhibitory synaptic plasticity in behaving mice. (**A**) Labeling strategy for the all-optical assay of CCKBC synaptic function in vivo. (**B**) Top: example unfiltered fluorescence traces from four CA1 neurons [(a) to (d)]. Bottom: spike raster (n = 30 neurons from n = 5 mice). Cyan bars indicate CCKBC photostimulation onset (488 nm, 10 ms duration, 9.5 to 20 mW/mm^2, 0.5 Hz). (**C**) Mean subthreshold postsynaptic waveforms after presynaptic CCKBC photostimulation (n = 30 neurons from n = 5 mice). (**D**) Unfiltered example traces of plateau-driven complex spikes (CS, red arrows) preceding photostimulation events. (**E**) Additional example traces from the same cells as in (D) without complex spikes occurring within 1 s before the stimulation. (**F**) Stimulus-triggered average (mean ± SEM) oeIPSP (black: with CS; orange: without CS). (**G**) Quantification of neuronal depolarization before stimulation and oeIPSP amplitudes (negative values) during trials with or without preceding complex spikes (depolarization: P = 0.0076, paired t test, n = 15 cells from n = 4 mice; oeIPSP amplitude: P = 0.0045). (**H**) Histograms of place field sizes of individual place cells in control mice and after cell-type-specific CB_1 KO in GABAergic neurons (GABA-CB_1-KO). n = 420 ± 254 place cells from n = 5 control and n = 3 GABA-CB_1-KO mice. (**I**) Quantification of place cell place field size and spatial information. n = 13 sessions from n = 2 male and n = 2 female control mice; n = 19 sessions from n = 3 male GABA-CB1-KO mice. Markers and box plots show individual sessions (boxes: median ± interquartile range, whiskers: nonoutlier range). Place field size: P = 0.032, $\chi^2(1)$ = 4.59; spatial information: P = 0.004, $\chi^2(1)$ = 8.5, linear mixed effects models and likelihood ratio test.

Postsynaptic activity–dependent modulation of inhibitory postsynaptic potentials

Retrograde eCB signaling through CB_1 inhibits CCKBC to pyramidal cell synapses in vitro (*9*, *31*). On the basis of our results showing eCB transients time-locked to calcium transients, we expected to observe an activity-dependent modulation of CCKBC synapses. We used a CCKBC-specific (Sncg-FlpO) mouse line to test this hypothesis (*32*) and developed an all-optical method to study synaptic transmission between CCKBCs and postsynaptic neurons. These animals express the FlpO recombinase enzyme specifically in gamma-synuclein (Sncg)–expressing cells. Sncg is expressed selectively in CCKBCs; therefore, FlpO will be expressed specifically in this cell population in Sncg-FlpO mice. We expressed FlpO-dependent excitatory opsin (sombC1C2TG) (*33*) in CCKBCs and a soma-localized genetically encoded voltage indicator (GEVI, somQuasAr6a) (*34*) in sparsely labeled CA1 neurons in Sncg-FlpO mice (Fig. 3A and fig. S3A). We imaged GEVI in awake mice head-fixed on a spherical treadmill while activating CCKBCs with photostimulation (Fig. 3B). Brief CCKBC activation elicited time-locked CA1 neuronal hyperpolarization, consistent with optogenetically evoked inhibitory postsynaptic potentials (oeIPSP; Fig. 3C).

Plateau-driven complex spikes in CA1 pyramidal cells are particularly important for synaptic plasticity (*12*, *33*, *35*). We identified plateau-driven complex spikes with voltage imaging and then grouped the photostimulation-induced responses based on the presence or absence of complex spikes during the 1 s before the stimulus (Fig. 3, D and E). Whereas oeIPSPs were detectable in the absence of a preceding complex spike (Fig. 3E), the same postsynaptic cells showed reduced oeIPSPs after complex spikes (Fig. 3, D, F, and G). As expected, the average postsynaptic depolarization before the CCKBCs stimulus was higher in the presence of complex spikes (Fig. 3G). Together, these results demonstrate a transient suppression of CCKBC inhibition after complex spikes, consistent with a DSI-like mechanism.

Interneuron cannabinoid receptors modulate place cell activity patterns

The above results provide evidence for postsynaptic neuronal activity–dependent modulation of CCKBC synapses in vivo. A suppression of inhibition could disinhibit place cells during place field traversal, contributing to location-specific place cell activity (*16*, *36*). To determine whether preventing inhibitory synaptic eCB signaling may lead to altered place fields, we knocked out CB_1 selectively in forebrain GABAergic neurons (GABA-CB_1-KO, lacking CB_1 from perisomatic and dendritic interneurons) (*28*) (fig. S3B) and recorded place cell calcium signals during a spatial navigation task as mice foraged for a water reward. Both control (Dlx-Cre) and GABA-CB_1-KO mice exhibited spatially tuned calcium signals, suggesting that CB_1 expression by GABAergic neurons is not required for place field formation per se (fig. S3, C and D). However, we observed a widening of place fields in GABA-CB_1-KO mice relative to mice with intact CB_1 expression (Fig. 3, H and I). Analyzing the properties of individual place cells revealed that in the absence of interneuron CB1 expression, place cells were active over a larger fraction of the belt and altogether encoded less spatial information (Fig. 3I and fig. S3, C to J). In GABA-CB_1-KO mice, place cells fired less reliably lap-to-lap, and had fewer calcium transients near the preferred location (fig. S3, H and I). As a population, place cells in the GABA-CB_1-KO encoded mouse location less accurately compared with control despite the similar ratio of place cells (fig. S3, E and J). The observed changes in place cell activity patterns are consistent with the reported impaired spatial learning performance of GABA-CB_1-KO mice (*37*) and mice with perturbed CCKBC development (*38*).

In this study, we report (i) rapid eCB signals time-locked to calcium transients in hippocampal neurons including place cells, both in the postsynaptic membrane and the presynaptic inhibitory axons; (ii) modulation of CCKBC synapses correlated to past postsynaptic activity; and (iii) diminished place cell place field properties in the absence of eCB signaling at inhibitory synapses. Our results demonstrate that an eCB-mediated, DSI-like plasticity is capable of rapid modulation of inhibition in vivo on the behaviorally relevant timescale of seconds. Because of the selective expression of CB_1 at synapses of CCK-expressing but not PV-expressing interneurons, DSI may enable recently activated place cells to maintain elevated excitability without suppressing the ability of PVBC synapses to synchronize the PC population activity dynamics to theta and gamma oscillations (*39*, *40*). Such a selective, lasting suppression of inhibition involving CB_1 signaling may also contribute to maintaining an eligibility trace for non-Hebbian activity–dependent plasticity (*41*).

REFERENCES AND NOTES

1. I. Llano, N. Leresche, A. Marty, *Neuron* **6**, 565–574 (1991).
2. T. A. Pitler, B. E. Alger, *J. Neurosci.* **12**, 4122–4132 (1992).
3. A. C. Kreitzer, W. G. Regehr, *J. Neurosci.* **21**, RC174 (2001).
4. R. I. Wilson, R. A. Nicoll, *Nature* **410**, 588–592 (2001).
5. T. Maejima, K. Hashimoto, T. Yoshida, A. Aiba, M. Kano, *Neuron* **31**, 463–475 (2001).
6. I. Katona *et al*., *J. Neurosci.* **19**, 4544–4558 (1999).
7. K. Tsou, S. Brown, M. C. Sañudo-Peña, K. Mackie, J. M. Walker, *Neuroscience* **83**, 393–411 (1998).
8. G. Marsicano, B. Lutz, *Eur. J. Neurosci.* **11**, 4213–4225 (1999).
9. C. Földy, A. Neu, M. V. Jones, I. Soltesz, *J. Neurosci.* **26**, 1465–1469 (2006).
10. S.-H. Lee *et al*., *J. Neurosci.* **35**, 10039–10057 (2015).
11. J. O'Keefe, J. Dostrovsky, *Brain Res.* **34**, 171–175 (1971).
12. K. C. Bittner *et al*., *Nat. Neurosci.* **18**, 1133–1142 (2015).
13. F. Dubruc, D. Dupret, O. Caillard, *J. Neurophysiol.* **110**, 1930–1944 (2013).
14. G. Carlson, Y. Wang, B. E. Alger, *Nat. Neurosci.* **5**, 723–724 (2002).
15. V. Chevaleyre, P. E. Castillo, *Neuron* **43**, 871–881 (2004).
16. M. Valero, A. Navas-Olive, L. M. de la Prida, G. Buzsáki, *Cell Rep.* **40**, 111232 (2022).
17. S. V. Rolotti *et al*., *Neuron* **110**, 783–794.e6 (2022).
18. T. F. Freund, I. Katona, D. Piomelli, *Physiol. Rev.* **83**, 1017–1066 (2003).
19. A. Dong *et al*., *Nat. Biotechnol.* **40**, 787–798 (2022).
20. J. S. Farrell *et al*., *Neuron* **109**, 2398–2403.e4 (2021).
21. Y. Hashimotodani, T. Ohno-Shosaku, M. Kano, *Curr. Opin. Neurobiol.* **17**, 360–365 (2007).
22. H. Dana *et al*., *eLife* **5**, e12727 (2016).
23. N. B. Danielson *et al*., *Neuron* **91**, 652–665 (2016).
24. P. Kaifosh, J. D. Zaremba, N. B. Danielson, A. Losonczy, *Front. Neuroinform.* **8**, 80 (2014).
25. Y. Hashimotodani, T. Ohno-Shosaku, T. Maejima, K. Fukami, M. Kano, *Neuropharmacology* **54**, 58–67 (2008).
26. J. Z. Long, D. K. Nomura, B. F. Cravatt, *Chem. Biol.* **16**, 744–753 (2009).
27. E. Albarran *et al*., *Nat. Neurosci.* **26**, 997–1007 (2023).
28. K. Monory *et al*., *Neuron* **51**, 455–466 (2006).
29. B. Dudok *et al*., *Nat. Neurosci.* **18**, 75–86 (2015).
30. B. Pan *et al*., *J. Pharmacol. Exp. Ther.* **331**, 591–597 (2009).
31. L. L. Glickfeld, M. Scanziani, *Nat. Neurosci.* **9**, 807–815 (2006).
32. B. Dudok *et al*., *Neuron* **109**, 997–1012.e9 (2021).
33. L. Z. Fan *et al*., *Cell* **186**, 543–559.e19 (2023).
34. H. Tian *et al*., *Nat. Methods* **20**, 1082–1094 (2023).
35. J. Epsztein, M. Brecht, A. K. Lee, *Neuron* **70**, 109–120 (2011).
36. S. Royer *et al*., *Nat. Neurosci.* **15**, 769–775 (2012).
37. Ö. Albayram, S. Passlick, A. Bilkei-Gorzo, A. Zimmer, C. Steinhäuser, *Pflugers Arch.* **468**, 727–737 (2016).
38. I. Del Pino *et al*., *Nat. Neurosci.* **20**, 784–792 (2017).
39. C. Varga, P. Golshani, I. Soltesz, *Proc. Natl. Acad. Sci. U.S.A.* **109**, E2726–E2734 (2012).
40. M. Bartos *et al*., *Proc. Natl. Acad. Sci. U.S.A.* **99**, 13222–13227 (2002).
41. A. D. Milstein *et al*., *eLife* **10**, e73046 (2021).

ACKNOWLEDGMENTS

We thank A. Ortiz, C. Porter, S. Linder, and K. Patron for technical and administrative support. **Funding:** This work was supported by the National Institute of Neurological Disorders and Stroke (NINDS) of the National Institutes of Health (NIH). The content is solely the responsibility of the authors and does not necessarily represent the official views of the NIH. This work was supported by the NIH (grants R01NS99457, R01NS131728, and R01NS133381 to I.S.; grant R00NS117795 to B.D.; grant K99MH132871 to L.Z.F.; and grant K99NS126725 to J.S.F.); the Knight Initiative for Brain Resilience (grant KCG-116 to I.S.); a McNair scholarship from the McNair Medical Institute at The Robert and Janice McNair Foundation to B.D.; a Helen Hay Whitney fellowship to L.Z.F.; a Burroughs Wellcome Fund Career Award at the Scientific Interface to L.Z.F.; a Stanford University Bio-X Undergraduate Summer Research Program grant to C.W.; and the National Institute of Mental Health, National Institute on Drug Abuse, National Science Foundation, Gatsby Foundation, Fresenius Foundation, AE Foundation, Tarlton Foundation, and NOMIS Foundation to K.D. **Author contributions:** Conceptualization: B.D., L.Z.F., K.D., I.S.; Formal analysis: B.D., L.Z.F.; Funding acquisition: B.D., K.D., I.S.; Investigation: B.D., L.Z.F., J.S.F., S.M., J.H., D.K., C.W., C.R.; Methodology: B.D., L.Z.F., J.S.F.; Resources: Y.L.; Supervision: K.D., I.S.; Visualization: B.D., L.Z.F.; Writing – original draft: B.D., L.Z.F., I.S.; Writing – review & editing: all authors. **Competing interests:** I.S. declares unrelated consultant activity for Actio Biosciences, CODA Biotherapeutics, MapLight Therapeutics, Praxis Precision Medicines, and Ray Therapeutics. K.D. declares unrelated consultant activity for MapLight Therapeutics and Stellaromics. The remaining authors declare no competing interests. **Data and materials availability:** All data, code, and materials are available from the authors upon reasonable request.

SUPPLEMENTARY MATERIALS

science.org/doi/10.1126/science.adk3863
Materials and Methods
Figs. S1 to S3
References (*42*–*45*)
MDAR Reproducibility Checklist

Submitted 18 August 2023; accepted 24 January 2024
10.1126/science.adk3863

Science
AAAS

Supplementary Materials for

Retrograde endocannabinoid signaling at inhibitory synapses in vivo

Barna Dudok *et al*.

Corresponding author: Barna Dudok, barna.dudok@bcm.edu

Science **383**, 967 (2024)
DOI: 10.1126/science.adk3863

The PDF file includes:

Other Supplementary Material for this manuscript includes the following:

Materials and Methods

Animals

All procedures were carried out in accordance with NIH guidelines and with the approval of the Administrative Panel on Laboratory Animal Care of Stanford University. Adult mice of both sexes (2 months and older) were used in all experiments, unless otherwise specified. Mice were housed in groups of 2-5 animals except if separation was necessitated by fighting, on a normal diet and 12/12 light/dark cycle. Mice used for voltage imaging were housed on reverse 12/12 light/dark cycle.

Wild type Bl6 mice were from JAX (000664). Sncg-FlpO mice (JAX: 034424) were bred as heterozygotes by crossing FlpO $^{+/-}$ mice with Bl6 mice. For generating double transgenic animals, floxed CB_1 (JAX:036107) and Dlx-Cre (JAX:008199) mice were crossed, and first-generation progeny (CB_1 $^{f/wt}$, Dlx-Cre $^{+/-}$) were bred with homozygous CB_1 $^{f/f}$ mice to generate cell type-specific knockouts (CB_1 $^{f/f}$, Cre $^{+/-}$).

Viral injections

Mice were anesthetized with isoflurane and treated with analgesics (bupivacaine and buprenorphine). The skull was exposed, and a hole was drilled above the right dorsal hippocampus. Mice were injected in the dorsal CA1 (2.3mm posterior, 1.5 mm lateral, 1.45-1.35mm ventral to Bregma) using a 1 microliter Neuros (Hamilton) syringe, with one or more of the following viruses: AAV1-Syn-NES-jRGECO1a-WPRE-SV40, AAV9-Syn-eCB2.0, AAV9-hSyn-DIO-eCB2.0, AAV9-EF1a-fDIO-mCherry, AAV8-Ef1a-fDIO-GCaMP6s (300-400 nl each, full titer). Injection was started ventrally, and virus was delivered in pulses of 50-100 nl while gradually raising the syringe within the dorsoventral range, with 1-minute intervals between pulses. Sncg-FlpO mice used for presynaptic calcium analyses also expressed a designer receptor (fDIO-hM4D(Gi)-mCherry) but were not treated with any drugs in the analyzed experiments.

For voltage imaging experiments, virus injections were made using home-pulled micropipettes (Sutter P1000 pipette puller), mounted in a microinjection pump (World Precision Instruments Nanoliter 2010) controlled by a microsyringe pump controller (World Precision Instruments Micro4). The micropipette was positioned using a stereotaxic instrument (Kopf Instruments). Virus comprised AAV2/9 hSyn-DIO-somQuasAr6a-EGFP (final concentration ~3-5×10^{11} GC/mL) mixed with AAV2/9 CKII(0.4)-Cre virus (final titer ~1×10^{10} GC/mL) and AAV2/8 hSyn-fDio-sombC1C2TG-P2A-tagBFP (final titer ~3-5×10^{11} GC/mL). Virus was injected in the right hippocampal CA1 (150 – 300 nl, 45 – 60 nL/min, AP: -2.0 mm, ML: 1.5 mm, DV: -1.35 mm).

Drug injections.

For analyzing the effect of 2-AG and AEA synthesis and degradation inhibitors, we used baseline (no seizure) data recorded in our previous study (*20*). Briefly, JZL184 and URB597 were obtained from Cayman Chemicals (Ann Arbor, MI), LEI401 was obtained from MedChemExpress (Monmouth Junction, NJ), and DO34 was obtained from Aobious (Gloucester, MA). Drugs were delivered through intraperitoneal injection in a vehicle composing of 1:1:18 of DMSO:Tween80:saline and injected at a volume of 3mL/kg at 30 minutes before recording. A minimum of 24 hours washout period was maintained between doses.

Fluorescent immunostaining

Mice were anaesthetized by isoflurane, then injected i.p. with ketamine (100 mg/kg) and xylazine (10 mg/kg) in saline. The animals were transcardially perfused with saline (9 ml 0.9% NaCl for 1 minute) and then with fixative solution (4% paraformaldehyde with 0.2% picric acid in 0.1 M phosphate buffer). The fixative volume was 40-100 ml for each mouse. Perfused brains

were then post-fixed in the same fixative for 24 h at 4°C. Brains were sliced on a vibratome (VT 1200 S, Leica Biosystems).

Immunostaining was carried out on free-floating coronal sections (50 μm). Sections were washed in 0.1 M phosphate buffer, blocked in 0.05 M tris-buffered saline (TBS) containing 0.3% Triton X-100 (Sigma-Aldrich) and 1% bovine serum albumin (Sigma-Aldrich). Sections were incubated overnight in a mix of primary antibodies diluted in TBS: chicken anti-GFP (1:3000, Aves, RRID: AB_10000240) and rabbit anti-CB1 (1:3000, Immunogenes, RRID: AB_2813823). After washing with TBS, sections were incubated in secondary antibodies diluted in TBS (1 μg/ml, conjugated with CF405S or CF488A, highly cross-absorbed, by Biotium). Sections were then washed and mounted on glass slides in Vectashield (Vector Laboratories).

Confocal images were acquired on a Zeiss LSM 800 confocal microscope using 10× 0.45 NA, 20× 0.8 NA, or 63× 1.4 NA objectives.

Imaging window surgery

For calcium imaging experiments, surgeries were performed after three days or more of postoperative recovery following viral injections. Mice were then surgically implanted with a glass imaging window (diameter: 3.0 mm, 64-0720, Warner), attached to a stainless steel cylindrical steel cannula (diameter: 3.0 mm, Tegra Medical, cut to 1.5 mm long pieces) with Narland optical adhesive. Mice were anesthetized with isoflurane and treated with analgesics (bupivacaine and buprenorphine), the skull was exposed, and a 3.0 mm diameter craniotomy was made with a hand-held drill. Dura and cortical layers were removed while flushing the brain with ice-cold cortex buffer (*42*), to minimize bleeding. The cannula was inserted, secured with tissue adhesive (Vetbond). The cannula and the exposed skull were covered with self-etching UV-curable adhesive (Optibond), and a stainless steel headpost was attached with dental cement (Teets). After postoperative recovery, mice returned to home cages enriched with an igloo and running wheel (Bio-Serv).

While the experiments in this study did not utilize electrical recordings, certain mice were implanted with chronic electrodes. A craniotomy was made, and mice were head-fixed on a spherical treadmill (Styrofoam ball). An electrode (twisted tungsten wire pair, 0.002", 0.5 mm tip separation, A-M systems) was lowered in the dorsal CA1 mirroring the virus injection site. The probe was stabilized using UV-curable glue, and the connector pins (A-M systems) were attached to the headbar implant with dental cement.

For voltage imaging experiments, the procedure for surgery and imaging in CA1 was based on the protocol from Dombeck et al (*43*). Mice were deeply anesthetized with 2% isoflurane and maintained with ~1% isoflurane throughout the surgery. Before the start of surgery, animals were subcutaneously administered buprenorphine sustained release (SR) (0.3-1.0 mg/kg), 1 ml saline, carprofen (5 mg/kg), and dexamethasone (4.8 mg/kg). Throughout the surgery, eyes were kept moist using ophthalmic eye ointment. Body temperature was continuously monitored and maintained at 37 °C using a heating pad. The skull was exposed and thoroughly dried.

Virus was injected and then a 3 mm round craniotomy (centered at AP: -2 mm, ML: 2 mm) was opened using a biopsy punch (Miltex). The dura was then gently removed, and the overlying cortex was aspirated using a blunt aspiration needle under constant irrigation with cold PBS. The center region of the external capsule was removed to expose hippocampal CA1. A cannula window was prepared prior to the surgery and comprised a 1.5 mm long stainless steel tube (3 mm outer diameter, MicroGroup) and 3 mm round #1 cover glass (Harvard Apparatus) glued together with UV curable adhesive (Norland Products, NOA 81). Once bleeding stopped, the cannula was then lowered onto the CA1 surface until the window touched the tissue. The remaining outer surface of

the cannula was sealed to the exposed skull with cyanoacrylate adhesive and dental cement that was dyed black using black ink (C&B metabond, Parkell, No. 242-3200). Finally, a stainless steel head plate was fixed onto the exposed skull. Animals were placed on a warming blanket to recover. Animals were typically active within 20 min and returned to their home cage for recovery. To avoid damage to the implant, mice were housed in separate cages. Mice were monitored for the next several days and given additional carprofen and buprenorphine if they showed signs of discomfort or infection. Mice were allowed to recover for ~7 days before beginning water restriction as a motivator to promote running behavior during recording.

In vivo two-photon calcium imaging

In vivo imaging was performed as previously described (*32*). A two-photon, 8 kHz resonant scanner microscope (Neurolabware), and a 16x objective (0.8 NA WI, Nikon) was used. Acquisition was controlled by Scanbox (Neurolabware). Recording sessions lasted 10-20 minutes, during which the mice were freely running and resting on a 2 m-long treadmill belt. For sessions in which place cells were recorded, the belt consisted of four different fabrics and decorated with tactile cues approximately every 30 cm. Treadmill position was recorded, and rewards were controlled by a system consisting of Arduino microcontrollers, custom electronics and software, that were synchronized to the image acquisition system. For experiments with a spatial navigation task, mice were housed water restricted and received their water daily during training or task performance. Water reward was provided by the automated system whenever mice licked the water port within a reward zone. Reward zones (2-4 per lap) were randomized either at the start of each lap, or at the start of each session. Both session types were pooled for analysis.

In vivo voltage imaging

Voltage imaging and optogenetic stimulation were performed on the custom-designed microscope described in Fan et al (33). Briefly, for voltage imaging, we used a spatial light modulator for targeted illumination of red light. For optogenetic stimulation, we delivered global optogenetic stimulation across a field of view of ~670 x ~890 μm through a digital micromirror device. Mice were imaged 1-3 months after virus injection and cranial window surgeries. Recordings targeting hippocampal CA1 neurons in vivo were performed at 1 kHz and at a depth of 100 – 250 μm.

Confocal image analysis

High-power images obtained with a 63x oil immersion objective were deconvolved using the CMLE algorithm of Huygens. For analyzing fluorescence intensity in individual boutons of genetically targeted interneurons, objects were segmented in the mCherry channel using the *scipy.ndimage* and *cv2* packages in Python. First, in each optical section, the image was binarized using an adaptive Gaussian threshold, objects were labeled after a binary fill holes operation, and filtered to include objects with > 1 square micron size. Next, voxels of included 2D objects were filled in a 3D binary volume, a second step of object labeling identified 3D objects, which were then filtered for size (> 1 cubic micron). Finally, fluorescent intensities of the input image were measured in each 3D object and in each channel.

Figures showing microscopy images were prepared using ImageJ and Adobe Photoshop. Image stacks were processed using the *Despeckle* and *Subtract background* functions in ImageJ, maximum intensity projections were then created and exported as 8-bit RGB images. Pseudocoloring and adjustments of gamma were performed for each channel using the *Hue* and *Curves* functions in Photoshop. Merged images were created using the 'screen' overlay mode in Photoshop, using 80-100% fill value for each channel depending on the color. All adjustments were made adhering to image integrity standards and were applied uniformly to the entire image.

Processing and analysis of 2-photon movies

Calcium and eCB movies were pre-processed, cells were segmented, and ΔF/F traces were computed in Python as described previously (*32*). Motion correction was performed using the calcium channel as reference, and regions of interest (ROIs) were detected in the calcium channel using SIMA (*24*). First, a segmentation movie was generated by taking 100 random epochs, each consisting of 100 frames (approx. 15.6 s) and including the average of each epoch as a frame in the segmentation movie. To generate somatic ROIS (postCA), first cells were detected using the *STICA* method of SIMA. Next, the dark nuclei of pyramidal cells were detected by running the *PlaneCA1PC* method of SIMA on the inverted segmentation movie. Each nuclear ROI was added to the set after binary dilation, unless they overlapped with a STICA ROI. ROIs were not matched across sessions. ΔF/F traces were computed using a polynomial fit of the trace as the time-dependent baseline as described previously (*32*), thus, negative ΔF/F values are possible.

Presynaptically detected eCB signals were lower compared to postsynaptically detected signals, likely due to a combination of the effects of lower sensor density in preeCB ROIs and the potentially higher eCB concentration at the postsynaptic source of synthesis compared to the presynapse.

Finding calcium peaks and analyzing transients

Calcium DF/F traces from each ROI were filtered with the *gaussian_filter* function of *scipy*, with the sigma parameter set to 3, and standardized using the *StandardScaler* function of *sklearn*. Peaks were detected using the *find_peaks* function of *scipy*, and filtered for >3 peak height. Then, event-triggered average activity of the raw (i.e. not gaussian-smoothed) DF/F trace was computed for each cell, and then averaged across cells from the same session. The session average trace was used to fit an exponential function to the portion of the trace following the maximum. Peak height was measured from a baseline (minimum of the averaged trace in the t – 5 s to t – 0.5 s window). Peak delay was determined as the location of the maximum relative to t = 0, and the decay time constant was calculated from the parameter of the exponential fit.

Identification of place cells and computing spatial tuning curves

Calcium DF/F traces were deconvolved using the *oasis* package and further analyzed using Python. First, in order to identify place cells, the mutual information between activity and location (each normalized between 0-1) was computed using histograms with 11 bins in each dimension, including only frames recorded during locomotion (speed > 0). The expected value was defined as the 95th percentile of mutual information values obtained by shuffling the list of the cell's DF/F values. Cells with greater than expected mutual information were included as place cells.

For determining each place cell's preferred location, spatially binned average activity was calculated. The linear track was divided into 25 equal, non-overlapping bins. For each bin and each cell, a distance-weighted average activity was computed. The weight for each data point location was computed from the unsigned distance of the belt position from the bin center, so that the weight exponentially decayed to ~50% in ~25% of the belt length. The cell's preferred location was the argmax of the distance-weighted averages.

Spatial tuning curves were computed using distance-weighted average activity in the place cell postCa and corresponding post- or preeCB ROIs, as described above, but with increased resolution (100 bins, approx. 2 cm each) and using the "raw" relative DF/F trace instead of deconvolved firing rates (so that the approach is applicable to both Ca and eCB traces). Tuning curves from all place cells were then rolled to align the place cells' preferred locations to the central bin. eCB shuffled tuning curves were obtained with the same method after shuffling the list of indices of the corresponding eCB ROI for each postCa ROI.

For quantification of response magnitudes, the average activity of each ROI was calculated by applying a Gaussian smoothing to the tuning curve, z-scoring it, and taking the value at the preferred location. Then, response magnitudes were averaged by animal. When comparing vehicle and drug conditions, the z-scoring step was omitted.

Analysis of place cell properties

Quantification of place cell properties was done on a cell-by-cell basis. Sessions with less than 5 laps were excluded. Place field size was determined from the gaussian-filtered (sigma = 1) spatial tuning curve (described above), by counting the number of bins in which the tuning curve height was above half maximum. Place cell location information was determined as above, normalized to the mean of the mutual information values obtained by shuffling. Fraction of place cell ROIs was determined by dividing the number of statistically significant place cells (see above) with the total number of cells. Cell signal-to-noise levels were determined as the 99th percentile of the z-scored trace. Fraction of laps with Ca transients were defined as the number of laps in which a place cell calcium peak over 3 SD was detected within 20 cm in either direction from the preferred location of the cell, divided by the number of times the mouse traversed the preferred location. Location decoding was performed on frames obtained during locomotion (speed > 0), using separate models for each lap. Location was binned in 40 bins (5 cm each), and place cell activity traces were smoothed by a 15-period (~1 s) exponentially weighted moving average, then standard scaled and floored at 0. For each lap, a multinomial naive Bayes classifier (*scikit-learn*) was trained on data from all other laps, and then position during the current lap was predicted from the observed neuronal activity. Absolute distances between actual and predicted locations were determined in every frame and then averaged.

Analysis of voltage imaging

Corrections for photobleaching and motion artifacts

Movies were first corrected for motion using the NoRMCorre algorithm (*44*). Movies were then corrected for photobleaching by dividing the movie by an exponential fit of the mean fluorescence.

Image segmentation and waveform extraction

We divided the movie into sub-movies comprising single cells and performed activity-based image segmentation separately in each sub-movie. Whereas correlations often arose between subthreshold voltages and out-of-focus background, we assumed that spiking was not correlated with background, and furthermore that the spatial footprint associated with spiking would be the same as for true subthreshold dynamics. For segmentation purposes, we first removed subthreshold signals via a 100 Hz high-pass filter; movies were then segmented semi-automatically using activity-based segmentation algorithms. Principal components analysis was followed by time-domain independent components analysis (PCA/ICA) (*45*). The spatial masks from PCA/ICA were then applied to the original movies without high-pass filtering to extract fluorescence traces.

Spike finding, spike removal, and scaling of fluorescence recordings

A simple threshold-and-maximum procedure was applied for spike detection. Fluorescence traces were first high-pass filtered, and initial threshold was set at 4x noise level. This threshold was then manually adjusted. For spike removal, spikes were digitally removed and replaced with linear interpolation of the surrounding data. Linear interpolations were performed between data-points 3 ms before and 6 ms after action potential peak. All fluorescence signals were normalized

to spike height. Average IPSP traces are shown after 5-sample gaussian filtering. Spikes were digitally removed before averaging. Endogenous background from the brain arising from optogenetic-wavelength illumination contributed to a small step-like increase of fluorescence during the light pulse.

Plateau-driven complex spikes

To identify plateau-driven complex spikes, we smoothed the action potential-deleted traces with a moving-average filter (20 ms window). Events were detected from the smoothed trace by threshold crossing at 40% of spike height. Only events that lasted longer than 20 ms and rose atop spiking bursts (3 spikes) were considered as plateau events. All fluorescence signals were normalized to spike height. For the same cells, we then classified the optogenetic stimulus events into two categories depending on the activity patterns of the postsynaptic neurons. The first category contained no complex spikes occurring within 1 sec before the onset of the optogenetic stimulus, while the second contained complex spikes occurring within 1 sec before the onset of the optogenetic stimulus. Optogenetic stimulus events with complex spikes atop were excluded to avoid confounds from altered driving forces for inhibitory inputs. Average depolarization was measured during 600 ms preceding the photostimulation onset. Average complex spike duration was 50 ± 3 ms (mean ± SEM), amplitude: 0.60 ± 0.02 spike height.

Classification of synaptic potentials in response to CCKBC stimulation

We calculated area under curve (AUC) of the mean fluorescence trace in response to CCKBC stimulus. Cells with AUC < 0 were classified as having inhibitory inputs and analyzed. For comparing oeIPSCs between photostimulation events with- or without a preceding CS, the baseline was set to the average of -20 to -1 ms relative to stimulation onset, and excluded the stimulation period; The IPSP amplitude was measured as the minimum height of the PSP measured between 1 to 15 ms after the stimulation pulse.

Statistical analysis and plotting

Statistical analysis was done with the *scipy* and *statsmodels* packages of Python. Plots were generated using *matplotlib* in Python and edited for style using Adobe Illustrator. Appropriate statistical tests were selected based on study design. Reported measures of central tendency and error are mean ± standard error, unless otherwise specified. Tests are 2-sided unless otherwise specified. Sample sizes don't reflect repeated measures. Probabilities of the null hypothesis $p < 0.05$ were judged to be statistically significant.

In order to investigate sex-specific differences in spatial tuning curves, linear mixed effects models were fitted on the ROI-wise data (Response ~ Sex + (1|Animal)) and compared using ANOVA to null models omitting sex. No sex-specific differences were found in the study; therefore, these analyses are not reported.

For statistical comparisons of place cell properties, we used linear mixed effects models on the session-wise averages (Response ~ Genotype + (1|Animal)) and compared using ANOVA to null models omitting Genotype.

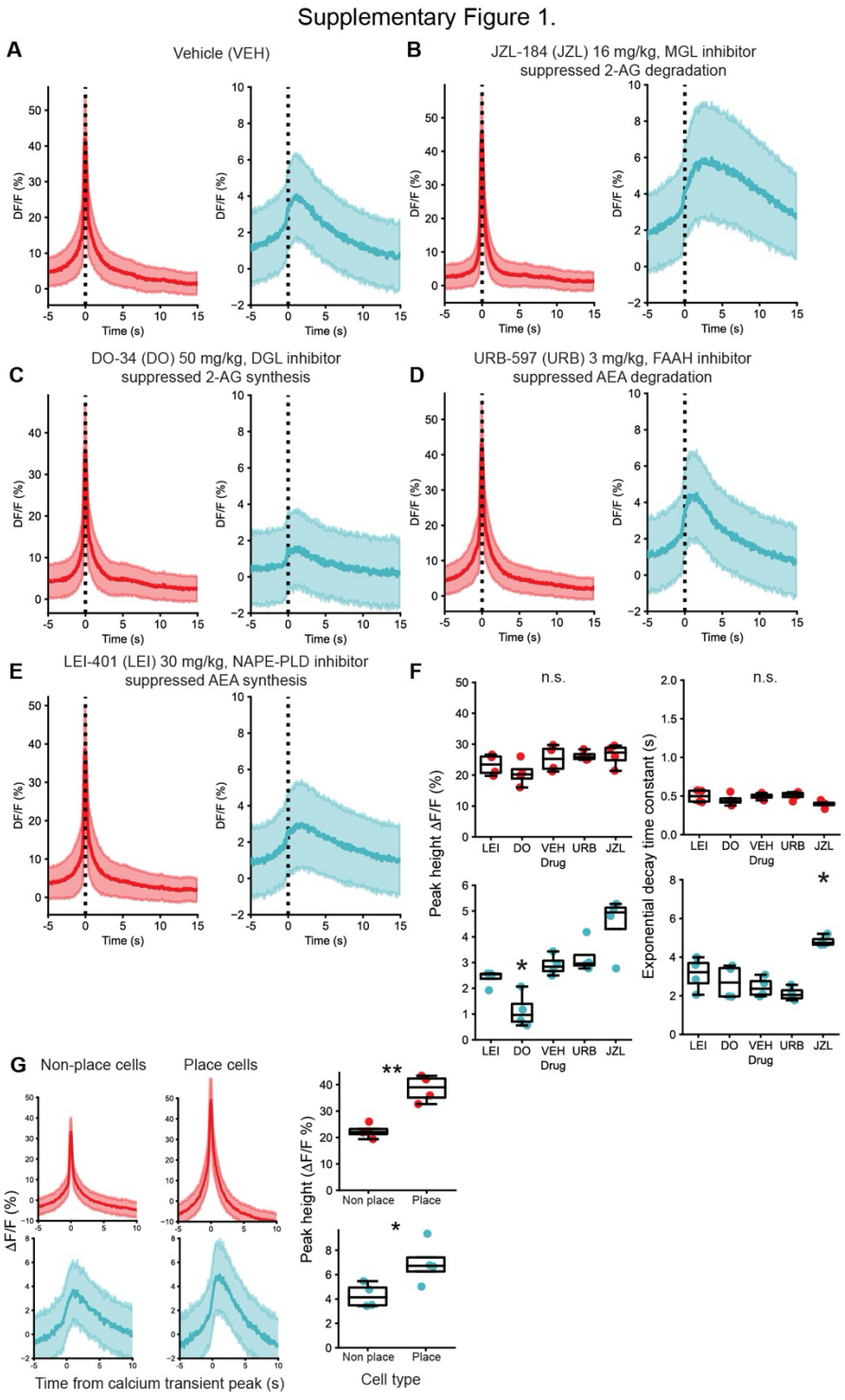

Fig. S1. Characterization of neuronal activity-related eCB signals after pharmacological manipulation of eCB metabolism

A) Calcium- and eCB transients in vehicle-injected mice. Same data as on Fig 1, reproduced here for comparison with drug-treated mice (B-E).

B) Calcium- and eCB transients after inhibiting 2-AG hydrolysis with a monoacylglycerol lipase (MAGL) inhibitor (JZL184, 16 mg/kg, i.p.)
C) Inhibiting 2-AG synthesis with a diacylglycerol lipase (DAGL) inhibitor (DO34, 50 mg/kg i.p.)
D) Inhibiting AEA hydrolysis with a fatty acid amide hydrolase (FAAH) inhibitor (URB597, 3 mg/kg i.p.)
E) Inhibiting AEA synthesis with a N-acylphosphatidylethanolamine phospholipase D (NAPE-PLD) inhibitor (LEI401, 30 mg/kg i.p.)
F) Quantification of calcium and eCB peak height and decay time constant. N = 4 mice. Multiple groups were compared using Kruskal-Wallis test: Ca peak height $p = 0.20$, $U = 6.0$; eCB peak height $p = 0.005$, $U = 14.8$; Ca decay constant $p = 0.18$, $U = 6.2$; eCB decay constant $p = 0.018$, $U = 12.0$. Drug conditions were compared to Vehicle using Dunn's post hoc test, asterisks indicate groups with $p < 0.05$.
G) Calcium- and eCB transients in drug-naive mice. Sessions were recorded on belts with cues, and place cells were identified. Place cell calcium and eCB transients were greater than transients in non-place cells (paired t test, n = 4 mice, Ca peak height $p = 0.0017$, $t = 10.75$; eCB peak height $p = 0.042$, $t = 3.42$).

Figure S2.

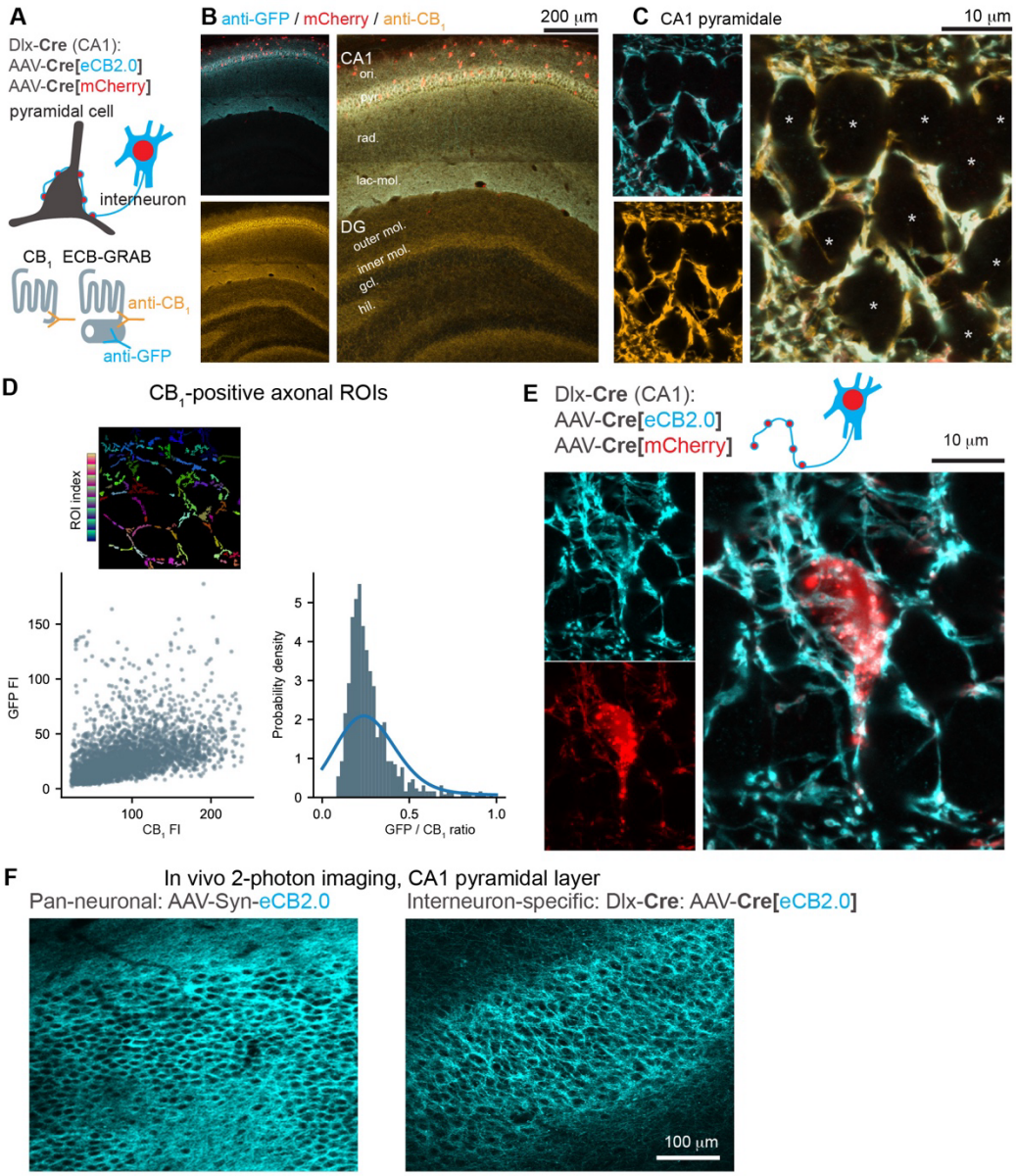

Fig. S2. Characterization of genetically encoded eCB reporter expression pattern in the hippocampus.

A) Strategy for $GRAB_{eCB2.0}$ expression and immunolabeling in hippocampal interneurons.

B) Confocal micrograph of the CA1 and dentate gyrus after immunostaining against $GRAB_{eCB2.0}$. Note the sparsely labeled interneuron somata in the CA1 and the enrichment of GFP-immunopositive ($GRAB_{eCB2.0}$-expressing) axons in the pyramidal layer. Representative of 3 mice. The anti-GFP immunostaining channel is shown in blue, mCherry is shown in red, and anti-CB1 is shown in orange. Note that anti-CB1 reveals both endogenous CB1 and $GRAB_{eCB2.0}$.

C) Deconvolved confocal micrograph of the pyramidal layer. Note the hollow, ring-like appearance of immunolabeling on mCherry-positive perisomatic axon terminals,

consistent with a membrane-targeted epitope. mCherry-negative somata (asterisks) were immunonegative for both GFP and CB_1.

D) Scatterplot of mean GFP and CB_1 immunostaining fluorescence intensity in automatically segmented CB_1-positive objects from Dlx-Cre mice (n = 3730 objects from 3 female Cre^+ mice) indicates no large population of CB_1-expressing, GFP-negative boutons. The insert on top shows an example z-section with individual objects colored according to their index. The histogram on the right shows unimodal distribution of the bouton-wise GFP/CB_1 ratios.

E) Deconvolved confocal micrograph of a mCherry-expressing (Cre-positive) neuron in the CA1 pyramidal layer, immunostained with anti-CB_1. Note the relatively weak immunoreactivity in the soma compared to nearby axons, indicating predominantly presynaptic eCB-GRAB expression.

F) Maximum intensity time projections of in vivo 2-photon imaging of pan-neuronal (left) or interneuron-specific (right) eCB-GRAB expression.

Figure S3.

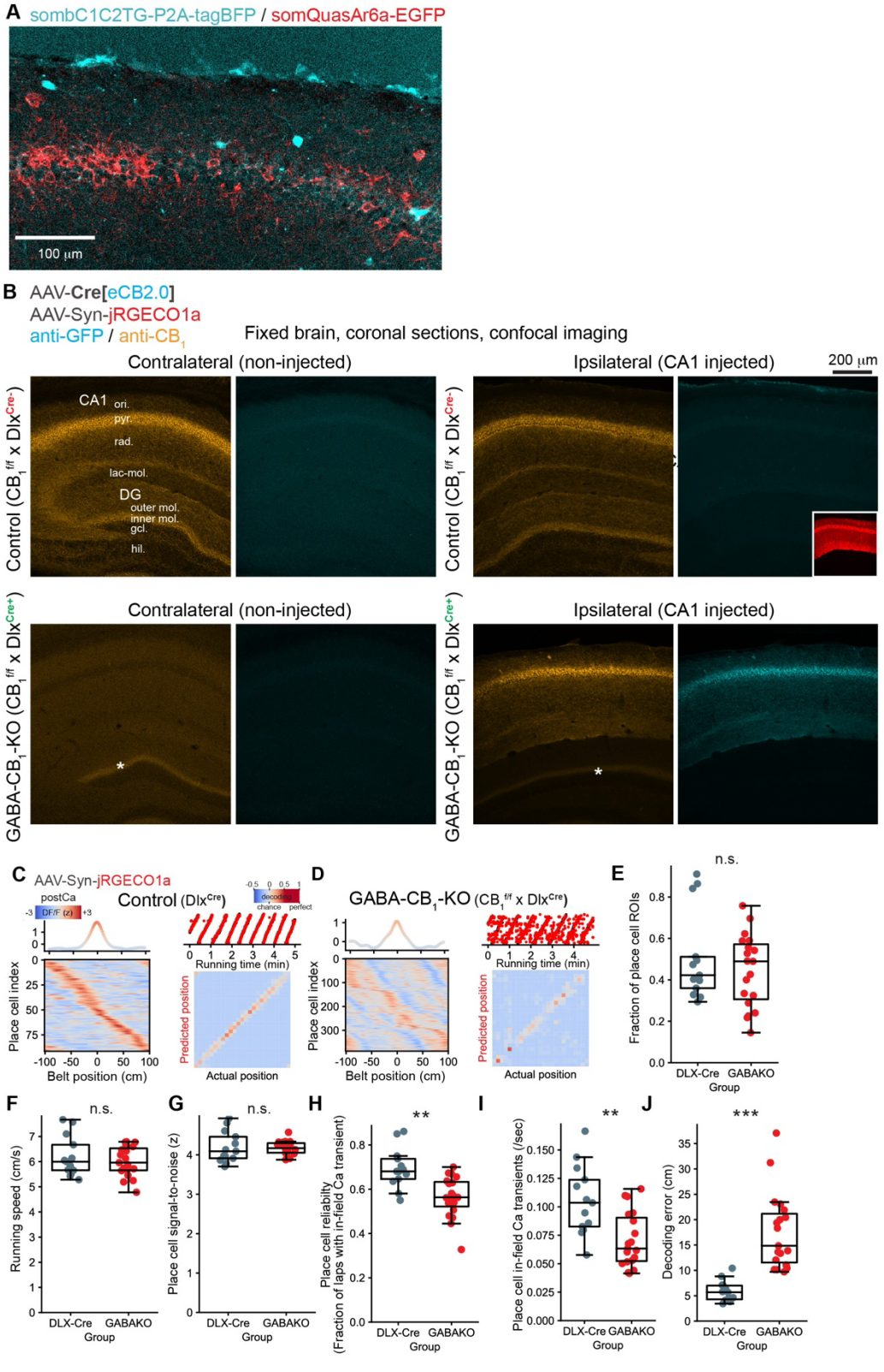
A sombC1C2TG-P2A-tagBFP / somQuasAr6a-EGFP
100 μm
B AAV-Cre[eCB2.0]
AAV-Syn-jRGECO1a
anti-GFP / anti-CB1
Fixed brain, coronal sections, confocal imaging
Contralateral (non-injected)
Ipsilateral (CA1 injected)
200 μm
Control (CB1 f/f x DlxCre-)
GABA-CB1-KO (CB1 f/f x DlxCre+)
CA1 ori.
pyr.
rad.
lac-mol.
DG
outer mol.
inner mol.
gcl.
hil.
C AAV-Syn-jRGECO1a
Control (DlxCre)
postCa
DF/F (z)
Place cell index
Belt position (cm)
Running time (min)
Predicted position
Actual position
decoding
chance
perfect
D GABA-CB1-KO (CB1 f/f x DlxCre)
E
Fraction of place cell ROIs
n.s.
DLX-Cre
GABAKO
Group
F
Running speed (cm/s)
G
Place cell signal-to-noise (z)
H
Place cell reliability
(Fraction of laps with in-field Ca transient)
**
I
Place cell in-field Ca transients (/sec)
J
Decoding error (cm)
***

Fig. S3. Characterization of genetically encoded voltage indicator expression patterns, and the effects of interneuron-specific CB1 deletion on hippocampal place cell properties.

A) Confocal image of fixed brain slices showing expression of somQuasAr6a (red) and sombC1C2TG (cyan) in CA1. Representative of n = 3 preparations

B) Confocal micrographs of anti-GFP and anti-CB1 immunostaining from conditional CB_1 knockout mice ($CB_1^{fl/fl}$) crossed with Dlx-Cre and injected with AAVs for conditional $GRAB_{eCB2.0}$ expression. A control littermate (Cre negative, top row, n=1 mouse) had normal CB_1 expression, but no $GRAB_{eCB2.0}$ expression (GFP immunoreactivity). The insert shows jRGECO expression, indicating successful AAV injection). Cre-expressing mice (bottom row, representative of 6 mice, 2 females, 4 males) show reduced endogenous CB1 expression in the contralateral CA1 (left column), due to CB_1 deletion in GABAergic interneurons. Note the remaining band of immunolabeling in the dentate molecular layer (asterisk), indicative of CB_1 expression in glutamatergic axons. AAV injection induced immunoreactivity with both anti-GFP and anti-CB_1 antibodies restricted to the injected CA1 (right column), indicating that $GRAB_{eCB2.0}$ contains both epitopes, and that the anti-CB_1 C-terminal antibody recognized both CB_1 and $GRAB_{eCB2.0}$, while the anti-GFP antibody labeled eCB-GRAB, but not CB_1.

C) Example sessions of postsynaptic calcium imaging in CA1 place cells. The left panel shows the location-averaged activity of place cells, ordered by preferred location. The top plot shows the average tuning curve aligned on preferred location. The right panels show location predicted by a classifier trained with holding out data from the current lap (red markers), overlaid on actual mouse location during running (black markers, often occluded). Decoder performance is also shown as histogram (bottom).

D) Same as (C) for GABA-CB_1-KO (cell type-specific CB_1 KO in GABAergic neurons).

E) The fraction of ROIs that were spatially selective was similar in both groups (control and GABA-CB_1-KO. n =13 sessions from 2 male and 2 female control mice; 19 sessions from 3 male GABA-CB1-KO mice. $p = 0.48$, $\chi^2 = 2.0$, linear mixed effects models and likelihood ratio test.

F) The running speed of mice was similar in both groups. $p = 0.44$, $\chi^2 = 0.6$.

G) The signal-to-noise of place cell $\Delta F/F$ traces was similar in both groups. $p = 0.56$, $\chi^2 = 0.3$.

H) In control mice, place cell calcium transients were detected in a higher fraction of place field traversals. $p = 0.0023$, $\chi^2 = 9.3$.

I) The rate of calcium transients within 20 cm distance from the preferred location was reduced in GABA-CB1-KO. $p = 0.0016$, $\chi^2 = 9.9$.

J) A decoder more accurately predicted animal location from place cell activity in control mice. $p = 0.0001$, $\chi^2 = 14.7$.

References and Notes

1. I. Llano, N. Leresche, A. Marty, Calcium entry increases the sensitivity of cerebellar Purkinje cells to applied GABA and decreases inhibitory synaptic currents. *Neuron* **6**, 565–574 (1991). doi:10.1016/0896-6273(91)90059-9 Medline

2. T. A. Pitler, B. E. Alger, Postsynaptic spike firing reduces synaptic GABAA responses in hippocampal pyramidal cells. *J. Neurosci.* **12**, 4122–4132 (1992). doi:10.1523/JNEUROSCI.12-10-04122.1992 Medline

3. A. C. Kreitzer, W. G. Regehr, Cerebellar depolarization-induced suppression of inhibition is mediated by endogenous cannabinoids. *J. Neurosci.* **21**, RC174 (2001). doi:10.1523/JNEUROSCI.21-20-j0005.2001 Medline

4. R. I. Wilson, R. A. Nicoll, Endogenous cannabinoids mediate retrograde signalling at hippocampal synapses. *Nature* **410**, 588–592 (2001). doi:10.1038/35069076 Medline

5. T. Maejima, K. Hashimoto, T. Yoshida, A. Aiba, M. Kano, Presynaptic inhibition caused by retrograde signal from metabotropic glutamate to cannabinoid receptors. *Neuron* **31**, 463–475 (2001). doi:10.1016/S0896-6273(01)00375-0 Medline

6. I. Katona, B. Sperlágh, A. Sík, A. Käfalvi, E. S. Vizi, K. Mackie, T. F. Freund, Presynaptically located CB1 cannabinoid receptors regulate GABA release from axon terminals of specific hippocampal interneurons. *J. Neurosci.* **19**, 4544–4558 (1999). doi:10.1523/JNEUROSCI.19-11-04544.1999 Medline

7. K. Tsou, S. Brown, M. C. Sañudo-Peña, K. Mackie, J. M. Walker, Immunohistochemical distribution of cannabinoid CB1 receptors in the rat central nervous system. *Neuroscience* **83**, 393–411 (1998). doi:10.1016/S0306-4522(97)00436-3 Medline

8. G. Marsicano, B. Lutz, Expression of the cannabinoid receptor CB1 in distinct neuronal subpopulations in the adult mouse forebrain. *Eur. J. Neurosci.* **11**, 4213–4225 (1999). doi:10.1046/j.1460-9568.1999.00847.x Medline

9. C. Földy, A. Neu, M. V. Jones, I. Soltesz, Presynaptic, activity-dependent modulation of cannabinoid type 1 receptor-mediated inhibition of GABA release. *J. Neurosci.* **26**, 1465–1469 (2006). doi:10.1523/JNEUROSCI.4587-05.2006 Medline

10. S.-H. Lee, M. Ledri, B. Tóth, I. Marchionni, C. M. Henstridge, B. Dudok, K. Kenesei, L. Barna, S. I. Szabó, T. Renkecz, M. Oberoi, M. Watanabe, C. L. Limoli, G. Horvai, I. Soltesz, I. Katona, Multiple forms of endocannabinoid and endovanilloid signaling regulate the tonic control of GABA release. *J. Neurosci.* **35**, 10039–10057 (2015). doi:10.1523/JNEUROSCI.4112-14.2015 Medline

11. J. O'Keefe, J. Dostrovsky, The hippocampus as a spatial map. Preliminary evidence from unit activity in the freely-moving rat. *Brain Res.* **34**, 171–175 (1971). doi:10.1016/0006-8993(71)90358-1 Medline

12. K. C. Bittner, C. Grienberger, S. P. Vaidya, A. D. Milstein, J. J. Macklin, J. Suh, S. Tonegawa, J. C. Magee, Conjunctive input processing drives feature selectivity in hippocampal CA1 neurons. *Nat. Neurosci.* **18**, 1133–1142 (2015). doi:10.1038/nn.4062 Medline

13. F. Dubruc, D. Dupret, O. Caillard, Self-tuning of inhibition by endocannabinoids shapes spike-time precision in CA1 pyramidal neurons. *J. Neurophysiol.* **110**, 1930–1944 (2013). doi:10.1152/jn.00099.2013 Medline

14. G. Carlson, Y. Wang, B. E. Alger, Endocannabinoids facilitate the induction of LTP in the hippocampus. *Nat. Neurosci.* **5**, 723–724 (2002). doi:10.1038/nn879 Medline

15. V. Chevaleyre, P. E. Castillo, Endocannabinoid-mediated metaplasticity in the hippocampus. *Neuron* **43**, 871–881 (2004). doi:10.1016/j.neuron.2004.08.036 Medline

16. M. Valero, A. Navas-Olive, L. M. de la Prida, G. Buzsáki, Inhibitory conductance controls place field dynamics in the hippocampus. *Cell Rep.* **40**, 111232 (2022). doi:10.1016/j.celrep.2022.111232 Medline

17. S. V. Rolotti, M. S. Ahmed, M. Szoboszlay, T. Geiller, A. Negrean, H. Blockus, K. C. Gonzalez, F. T. Sparks, A. S. Solis Canales, A. L. Tuttman, D. S. Peterka, B. V. Zemelman, F. Polleux, A. Losonczy, Local feedback inhibition tightly controls rapid formation of hippocampal place fields. *Neuron* **110**, 783–794.e6 (2022). doi:10.1016/j.neuron.2021.12.003 Medline

18. T. F. Freund, I. Katona, D. Piomelli, Role of endogenous cannabinoids in synaptic signaling. *Physiol. Rev.* **83**, 1017–1066 (2003). doi:10.1152/physrev.00004.2003 Medline

19. A. Dong, K. He, B. Dudok, J. S. Farrell, W. Guan, D. J. Liput, H. L. Puhl, R. Cai, H. Wang, J. Duan, E. Albarran, J. Ding, D. M. Lovinger, B. Li, I. Soltesz, Y. Li, A fluorescent sensor for spatiotemporally resolved imaging of endocannabinoid dynamics in vivo. *Nat. Biotechnol.* **40**, 787–798 (2022). doi:10.1038/s41587-021-01074-4 Medline

20. J. S. Farrell, R. Colangeli, A. Dong, A. G. George, K. Addo-Osafo, P. J. Kingsley, M. Morena, M. D. Wolff, B. Dudok, K. He, T. A. Patrick, K. A. Sharkey, S. Patel, L. J. Marnett, M. N. Hill, Y. Li, G. C. Teskey, I. Soltesz, In vivo endocannabinoid dynamics at the timescale of physiological and pathological neural activity. *Neuron* **109**, 2398–2403.e4 (2021). doi:10.1016/j.neuron.2021.05.026 Medline

21. Y. Hashimotodani, T. Ohno-Shosaku, M. Kano, Ca(2+)-assisted receptor-driven endocannabinoid release: Mechanisms that associate presynaptic and postsynaptic activities. *Curr. Opin. Neurobiol.* **17**, 360–365 (2007). doi:10.1016/j.conb.2007.03.012 Medline

22. H. Dana, B. Mohar, Y. Sun, S. Narayan, A. Gordus, J. P. Hasseman, G. Tsegaye, G. T. Holt, A. Hu, D. Walpita, R. Patel, J. J. Macklin, C. I. Bargmann, M. B. Ahrens, E. R. Schreiter, V. Jayaraman, L. L. Looger, K. Svoboda, D. S. Kim, Sensitive red protein calcium indicators for imaging neural activity. *eLife* **5**, e12727 (2016). doi:10.7554/eLife.12727 Medline

23. N. B. Danielson, J. D. Zaremba, P. Kaifosh, J. Bowler, M. Ladow, A. Losonczy, Sublayer-specific coding dynamics during spatial navigation and learning in hippocampal area CA1. *Neuron* **91**, 652–665 (2016). doi:10.1016/j.neuron.2016.06.020 Medline

24. P. Kaifosh, J. D. Zaremba, N. B. Danielson, A. Losonczy, SIMA: Python software for analysis of dynamic fluorescence imaging data. *Front. Neuroinform.* **8**, 80 (2014). doi:10.3389/fninf.2014.00080 Medline

25. Y. Hashimotodani, T. Ohno-Shosaku, T. Maejima, K. Fukami, M. Kano, Pharmacological evidence for the involvement of diacylglycerol lipase in depolarization-induced endocanabinoid release. *Neuropharmacology* **54**, 58–67 (2008). doi:10.1016/j.neuropharm.2007.06.002 Medline

26. J. Z. Long, D. K. Nomura, B. F. Cravatt, Characterization of monoacylglycerol lipase inhibition reveals differences in central and peripheral endocannabinoid metabolism. *Chem. Biol.* **16**, 744–753 (2009). doi:10.1016/j.chembiol.2009.05.009 Medline

27. E. Albarran, Y. Sun, Y. Liu, K. Raju, A. Dong, Y. Li, S. Wang, T. C. Südhof, J. B. Ding, Postsynaptic synucleins mediate endocannabinoid signaling. *Nat. Neurosci.* **26**, 997–1007 (2023). doi:10.1038/s41593-023-01345-0 Medline

28. K. Monory, F. Massa, M. Egertová, M. Eder, H. Blaudzun, R. Westenbroek, W. Kelsch, W. Jacob, R. Marsch, M. Ekker, J. Long, J. L. Rubenstein, S. Goebbels, K.-A. Nave, M. During, M. Klugmann, B. Wölfel, H.-U. Dodt, W. Zieglgänsberger, C. T. Wotjak, K. Mackie, M. R. Elphick, G. Marsicano, B. Lutz, The endocannabinoid system controls key epileptogenic circuits in the hippocampus. *Neuron* **51**, 455–466 (2006). doi:10.1016/j.neuron.2006.07.006 Medline

29. B. Dudok, L. Barna, M. Ledri, S. I. Szabó, E. Szabadits, B. Pintér, S. G. Woodhams, C. M. Henstridge, G. Y. Balla, R. Nyilas, C. Varga, S.-H. Lee, M. Matolcsi, J. Cervenak, I. Kacskovics, M. Watanabe, C. Sagheddu, M. Melis, M. Pistis, I. Soltesz, I. Katona, Cell-specific STORM super-resolution imaging reveals nanoscale organization of cannabinoid signaling. *Nat. Neurosci.* **18**, 75–86 (2015). doi:10.1038/nn.3892 Medline

30. B. Pan, W. Wang, J. Z. Long, D. Sun, C. J. Hillard, B. F. Cravatt, Q. S. Liu, Blockade of 2-arachidonoylglycerol hydrolysis by selective monoacylglycerol lipase inhibitor 4-nitrophenyl 4-(dibenzo[d][1,3]dioxol-5-yl(hydroxy)methyl)piperidine-1-carboxylate (JZL184) Enhances retrograde endocannabinoid signaling. *J. Pharmacol. Exp. Ther.* **331**, 591–597 (2009). doi:10.1124/jpet.109.158162 Medline

31. L. L. Glickfeld, M. Scanziani, Distinct timing in the activity of cannabinoid-sensitive and cannabinoid-insensitive basket cells. *Nat. Neurosci.* **9**, 807–815 (2006). doi:10.1038/nn1688 Medline

32. B. Dudok, P. M. Klein, E. Hwaun, B. R. Lee, Z. Yao, O. Fong, J. C. Bowler, S. Terada, F. T. Sparks, G. G. Szabo, J. S. Farrell, J. Berg, T. L. Daigle, B. Tasic, J. Dimidschstein, G. Fishell, A. Losonczy, H. Zeng, I. Soltesz, Alternating sources of perisomatic inhibition during behavior. *Neuron* **109**, 997–1012.e9 (2021). doi:10.1016/j.neuron.2021.01.003 Medline

33. L. Z. Fan, D. K. Kim, J. H. Jennings, H. Tian, P. Y. Wang, C. Ramakrishnan, S. Randles, Y. Sun, E. Thadhani, Y. S. Kim, S. Quirin, L. Giocomo, A. E. Cohen, K. Deisseroth, All-optical physiology resolves a synaptic basis for behavioral timescale plasticity. *Cell* **186**, 543–559.e19 (2023). doi:10.1016/j.cell.2022.12.035 Medline

34. H. Tian, H. C. Davis, J. D. Wong-Campos, P. Park, L. Z. Fan, B. Gmeiner, S. Begum, C. A. Werley, G. B. Borja, H. Upadhyay, H. Shah, J. Jacques, Y. Qi, V. Parot, K. Deisseroth, A. E. Cohen, Video-based pooled screening yields improved far-red genetically encoded voltage indicators. *Nat. Methods* **20**, 1082–1094 (2023). doi:10.1038/s41592-022-01743-5 Medline

35. J. Epsztein, M. Brecht, A. K. Lee, Intracellular determinants of hippocampal CA1 place and silent cell activity in a novel environment. *Neuron* **70**, 109–120 (2011). doi:10.1016/j.neuron.2011.03.006 Medline

36. S. Royer, B. V. Zemelman, A. Losonczy, J. Kim, F. Chance, J. C. Magee, G. Buzsáki, Control of timing, rate and bursts of hippocampal place cells by dendritic and somatic inhibition. *Nat. Neurosci.* **15**, 769–775 (2012). doi:10.1038/nn.3077 Medline

37. Ö. Albayram, S. Passlick, A. Bilkei-Gorzo, A. Zimmer, C. Steinhäuser, Physiological impact of CB1 receptor expression by hippocampal GABAergic interneurons. *Pflugers Arch.* **468**, 727–737 (2016). doi:10.1007/s00424-015-1782-5 Medline

38. I. Del Pino, J. R. Brotons-Mas, A. Marques-Smith, A. Marighetto, A. Frick, O. Marín, B. Rico, Abnormal wiring of CCK^+ basket cells disrupts spatial information coding. *Nat. Neurosci.* **20**, 784–792 (2017). doi:10.1038/nn.4544 Medline

39. C. Varga, P. Golshani, I. Soltesz, Frequency-invariant temporal ordering of interneuronal discharges during hippocampal oscillations in awake mice. *Proc. Natl. Acad. Sci. U.S.A.* **109**, E2726–E2734 (2012). doi:10.1073/pnas.1210929109 Medline

40. M. Bartos, I. Vida, M. Frotscher, A. Meyer, H. Monyer, J. R. P. Geiger, P. Jonas, Fast synaptic inhibition promotes synchronized gamma oscillations in hippocampal interneuron networks. *Proc. Natl. Acad. Sci. U.S.A.* **99**, 13222–13227 (2002). doi:10.1073/pnas.192233099 Medline

41. A. D. Milstein, Y. Li, K. C. Bittner, C. Grienberger, I. Soltesz, J. C. Magee, S. Romani, Bidirectional synaptic plasticity rapidly modifies hippocampal representations. *eLife* **10**, e73046 (2021). doi:10.7554/eLife.73046 Medline

42. A. Holtmaat, T. Bonhoeffer, D. K. Chow, J. Chuckowree, V. De Paola, S. B. Hofer, M. Hübener, T. Keck, G. Knott, W.-C. A. Lee, R. Mostany, T. D. Mrsic-Flogel, E. Nedivi, C. Portera-Cailliau, K. Svoboda, J. T. Trachtenberg, L. Wilbrecht, Long-term, high-resolution imaging in the mouse neocortex through a chronic cranial window. *Nat. Protoc.* **4**, 1128–1144 (2009). doi:10.1038/nprot.2009.89 Medline

43. D. A. Dombeck, C. D. Harvey, L. Tian, L. L. Looger, D. W. Tank, Functional imaging of hippocampal place cells at cellular resolution during virtual navigation. *Nat. Neurosci.* **13**, 1433–1440 (2010). doi:10.1038/nn.2648 Medline

44. E. A. Pnevmatikakis, A. Giovannucci, NoRMCorre: An online algorithm for piecewise rigid motion correction of calcium imaging data. *J. Neurosci. Methods* **291**, 83–94 (2017). doi:10.1016/j.jneumeth.2017.07.031 Medline

45. E. A. Mukamel, A. Nimmerjahn, M. J. Schnitzer, Automated analysis of cellular signals from large-scale calcium imaging data. *Neuron* **63**, 747–760 (2009). doi:10.1016/j.neuron.2009.08.009 Medline